

# CCS Imaging of the Starless Core L1544: An Envelope with Infall and Rotation

Nagayoshi Ohashi and Siow Wang Lee

Academia Sinica Institute of Astronomy & Astrophysics

P.O. Box 1-87, Nankang, Taipei 115, Taiwan; ohashi@asiaa.sinica.edu.tw

David J. Wilner

Harvard-Smithsonian Center for Astrophysics, MS 42

60 Garden St., Cambridge, MA 02318

and

Masahiko Hayashi

Subaru Telescope, 650 North Aohoku Place, Hilo, HI 96720

## ABSTRACT

We have carried out observations of the starless core L1544 in the CCS ( $J_N = 3_2 - 2_1$ ) line at 9 millimeters wavelength using the BIMA array. The maps show an elongated condensation,  $0.15 \times 0.045$  pc in size, with stronger emission at the edges. The appearance is consistent with a flattened, ringlike structure viewed at high inclination to the line of sight. The CCS molecule is likely heavily depleted in the inner part of the core. The position velocity diagram along the major axis shows a remarkable pattern, a “tilted ellipse”, that can be reproduced by a simple model ring with motions of both infall and rotation. The models suggest comparable velocities for infall and rotation,  $\sim 0.1$  km s $^{-1}$ , in the outermost envelope, at radius 15000 AU.

*Subject headings:* ISM: individual (L1544) — ISM: kinematics and dynamics — stars: formation

## 1. Introduction

Radio and infrared observations have revealed that stars are formed in dense cloud cores (e.g., Beichman et al. 1986, Myers et al. 1987). From these observations as well as theoretical works, models of protostellar evolution for low-mass stars, from embedded protostars to visible T Tauri stars, have been proposed (e.g., Shu, Adams, & Lizano 1987). Recently, even kinematic evidence

for the infall of dense cores around embedded sources is observed (e.g., Zhou et al. 1993; Hayashi, Ohashi, & Miyama 1993). Although our understanding of the embedded and T Tauri phases has made great progress, the earliest stage of star formation or even a prior stage to star formation has still been poorly understood.

Dense cores without any detectable young stellar objects, i.e., starless dense cores are most probably sites where star formation has just started or will soon start. Although some dense cores, such as B 335 (Zhou et al. 1990), have been found to be a very early collapse phase, even in this case significant material has already collapsed onto the central star. Starless cores are therefore good targets to study the earliest stage of star formation. L1544 is a well-studied starless core in Taurus, observed in several line emissions such as  $\text{NH}_3$ , CS, and  $\text{N}_2\text{H}^+$  (e.g., Benson & Myers 1989, Tafalla et al. 1998; hereafter T98, Williams et al. 1999; hereafter W99) and submillimeter continuum (Ward-Thompson et al. 1994). Their observations were, however, made mainly using single-dish telescopes, which prevented them from studying detailed geometrical and kinematical structures of L1544. In addition, most of the emission lines they used were optically thick, resulting in difficulty in investigating the whole velocity structure without suffering self-absorption.

In this Letter, we report results of interferometric observations of the L1544 starless core in CCS ( $J_N = 3_2 - 2_1$ ). This transition of CCS will be excited in cold cores such as starless cores because of its low energy level ( $E_u \sim 3.2$  K; Yamamoto et al. 1990). Interferometric observations enable us to study geometrical and kinematical structures of L1544 in detail. In addition, CCS in L1544 is optically thin (see §2). Moreover, CCS is one of the carbon chain molecules that are more abundant in starless cores (Suzuki et al. 1992), and have no hyperfine structures, meaning that it is a good probe to study geometrical and kinematical structures of starless cores in detail (Langer et al. 1995, Kuiper, Langer, & Velusamy 1996, Wolkovitch et al. 1997).

## 2. Observations

Observations were made using the nine-antenna Berkeley-Illinois-Maryland Association (BIMA) array <sup>1</sup> in September 1998. We observed CCS ( $J_N = 3_2 - 2_1$ ), which has rest frequency of 33.751374 GHz (Yamamoto et al. 1990), with low-noise receivers utilizing cooled HEMT amplifiers, developed for observations of the Sunyaev-Zeldovich effect (Carlstrom, Marshall, & Grego 1996). The field of view of the array is  $\sim 5'$  at this frequency. Such a wide field of view is of great advantage to the imaging of L1544, which is moderately extended (see T98). The typical system temperature during the observations was 40-60 K in Single-side-band. Spectral information was obtained using a digital correlator with 1024 channels at a bandwidth of 6.25 MHz, providing a velocity resolution of  $\sim 0.054$  km s<sup>-1</sup> at the observed frequency. Two different configurations of

---

<sup>1</sup>Operated by the University of California at Berkeley, the University of Illinois, and the University of Maryland, with support from the National Science Foundation.

the array were used. Projected baselines ranged from 6 m to 240 m, so that the observations were not sensitive to structures extended more than  $\sim 5'$ , corresponding to 42000 AU at the distance of Taurus ( $d = 140$  pc; Elias 1978)<sup>2</sup>. The obtained channel data was reduced using the MIRIAD package. The phase was calibrated by observing 0530+135, and the complex passband of each baseline was determined from observations of 3C84. When CCS maps were made and cleaned, a Gaussian taper was applied to the visibility data to improve sensitivity to extended low brightness emission, so that the resultant beam size was  $20'' \times 13''$  with a position angle of  $-5^\circ$ . The resultant  $1 \sigma$  rms noise level for channel maps was typically  $0.165 \text{ Jy beam}^{-1}$ , equivalent to  $\sim 0.7 \text{ K}$  in brightness.

In order to measure the optical depth of CCS in L1544, we also observed CCS and  $\text{CC}^{34}\text{S}$  ( $J_N = 3_2 - 2_1$ ) simultaneously using the Nobeyama 45 m telescope ( $\Delta\theta \sim 52''$ ) in April 1999.  $T_A^*$  of CCS was measured to be 1.1 K, while no  $\text{CC}^{34}\text{S}$  emission was detected to a  $3 \sigma$  level of 0.072 K in  $T_A^*$ , indicating that a  $3 \sigma$  upper limit to the optical depth of CCS is 0.93 when the sulfur isotope ratio is the terrestrial value, 23. In this Letter, we will discuss results of the BIMA observations in detail.

### 3. Results

CCS was detected at the LSR velocities ranging from 6.88 to 7.48  $\text{km s}^{-1}$  with high S/N ( $\geq 3\sigma$ ). Figure 1 shows the CCS total intensity map, integrated over this velocity range. The map shows a structure elongated in the northwest-southeast direction (PA  $\sim 144^\circ$ ), with a size of  $\sim 210'' \times 64''$  at the  $3 \sigma$  level, corresponding to  $0.15 \times 0.045$  pc at the distance to Taurus. The ratio between the major and minor axes is  $\sim 3.3$ . The condensation consists of two blobs, one at the northwest and the other at the southeast, and each blob contains several peaks, suggesting that the condensation has clumpy structures.

A similar elongated structure was also observed in  $\text{N}_2\text{H}^+$  (W99), whereas it shows a smaller size ( $7000 \text{ AU} \times 3000 \text{ AU}$ ) and a slightly large position angle (PA  $= 155^\circ$ ). More interestingly, the CCS map does not show a prominent peak at the central part of the condensation (marked by the cross in Fig. 1), where the other maps taken in  $\text{C}^{34}\text{S}$  (2-1),  $\text{N}_2\text{H}^+$  (1-0), and  $800 \mu\text{m}$  show prominent peaks (T98, W99, Ward-Thompson et al. 1994). This difference suggests that the CCS in L1544 traces the outer regions of the core while the other molecules and dust trace the inner part.

The clumpy structures of the CCS condensation are more obvious in the channel maps as shown in the left panels of Fig. 2. Remarkable characteristics of the clumps are their narrow line width: each clump is detected at only a few velocity channels. This is shown in the right panels of Fig. 2, where line profiles of two representative clumps are presented. The line widths

---

<sup>2</sup>Note that the observations are less sensitive to the structures close to  $5'$  in extent (see Wilner & Welch 1994)

deconvolved with the instrumental velocity resolution ( $0.054 \text{ km s}^{-1}$ ) of the clumps were measured to be  $(0.06 \pm 0.01) - (0.13 \pm 0.01) \text{ km s}^{-1}$  in full width at half-maximum, which are almost equivalent to the thermal line width of the CCS molecule at 10 K or  $0.09 \text{ km s}^{-1}$  (see Langer et al. 1995), suggesting that thermal motions are dominant in the clumps. Note that the line profiles of the clumps often show double peaks. This is because two clumps with different peak LSR velocities partially coincide with each other. The multi-peak-velocity structure of L1544 was also observed in  $\text{C}^{34}\text{S}$  (T98). Physical properties of the clumps will be discussed in detail in a forth coming paper.

We discern the global velocity field of the CCS condensation from position-velocity diagrams (Fig. 3). Two velocity components are visible along the projected minor axis of the condensation (Fig. 3a): one at  $V_{\text{LSR}} \sim 7.1 \text{ km s}^{-1}$  and the other at  $V_{\text{LSR}} \sim 7.4 \text{ km s}^{-1}$ . Both components persist all along the minor axis except at the southwestern edge, where only the  $7.4 \text{ km s}^{-1}$  component is detected, and at the northeastern edge, where only the  $7.1 \text{ km s}^{-1}$  component is detected. This suggests that the two velocity components are mostly coincident along the line-of-sight. Neither velocity component shows any significant gradient along the minor axis.

The PV diagram along the projected major axis (Fig. 3b) shows more remarkable velocity structures. Similar to the PV diagram along the minor axis, there are two velocity components in the inner parts of the condensation ( $-40'' \leq \Delta x \leq +40''$  in Fig. 3b), whereas these two components merged into a single velocity component at each of the southeastern and northwestern edges of the condensation. The velocity difference between the two velocity components at  $\Delta x = 0''$  is  $\sim 0.25 \text{ km s}^{-1}$ , similar to that in Fig. 3a. In addition, a global velocity gradient,  $\sim 0.08 \text{ km s}^{-1}$  per 14000 AU, is observed from the southeast to the northwest. The  $\text{N}_2\text{H}^+$  observations (W99) also showed a velocity gradient at inner parts of L1544 along almost the same direction (PA=155°) although their measurements showed a  $\sim 3$  times larger gradient. Thus, the whole velocity structure of the CCS condensation can be represented as a “tilted ellipse”, as shown by the dashed curve in Fig. 3b. The elliptical velocity structure is roughly symmetrical with respect to  $V_{\text{LSR}} \sim 7.25 \text{ km s}^{-1}$ , suggesting that this velocity seems to be the systemic velocity of this system. This suggests that the two velocity components seen in Fig. 3a are actually blueshifted and redshifted parts in a single kinematical system. The global velocity gradient seen along the projected major axis suggests rotation of the CCS condensation, while the blueshifted and redshifted components overlapping with each other along the line of sight can be explained by inward motions in the condensation (see §4.2.).

## 4. Discussion

### 4.1. Geometrical Structures of the CCS Condensation

The elongated structure seen in the CCS total intensity map suggests that the CCS condensation has either a filamentary structure or a flattened one with an almost edge-on

configuration. The latter case is more likely in view of the high column densities needed to produce the self-absorption features observed in optically thick molecular tracers such as CS (T98) or  $\text{N}_2\text{H}^+$  (W99). The envelopes around young stellar objects (YSOs) often show flattened structures similar to the CCS condensation here except that their sizes are smaller (e.g., Ohashi et al. 1997). This fact suggests that flattened envelopes are present even before the YSOs form. The flattened geometry of starless cores are predicted by some theoretical simulations (e.g., Nakamura, Hanawa, & Nakano 1995, Matsumoto, Hanawa, & Nakamura 1997), in which magnetic fields or rotation play an important role in producing flattened structures. Note that magnetic fields may be more important to explain the flattened geometry of CCS because of its slow rotation (see §4.2.; see also W99). For the L1544 CCS condensation, the ratio between the projected major and minor axes implies an inclination angle of  $\sim 73^\circ$  ( $0^\circ$  for the face-on case) if it is spatially thin. If the flattened condensation is spatially thick like the envelopes around YSOs (e.g., L1527; Ohashi et al. 1997), then this estimate is a lower limit to the true inclination.

As pointed out in §3, the CCS total intensity is stronger at the northwestern and southeastern edges of the condensation, and weaker in the center. A ringlike geometry for the condensation, observed almost edge-on, is consistent with this pattern, since, for optically thin emission, the total intensity is proportional to the column density as long as there is no significant gradient in the excitation. As we will show in the next section, the velocity field also suggests a ringlike geometry for the condensation. Note that the CCS ring is not a physical structure but rather probably results from a lower abundance of CCS towards the center of the L1544 core. Most other tracers, including  $\text{C}^{34}\text{S}$ ,  $\text{N}_2\text{H}^+$ , and submillimeter dust continuum, show prominent peaks close to the center of the L1544 core. A similar situation has been observed in L1498, another starless core in Taurus, where CCS is weak toward the dust continuum peak (Kuiper et al. 1996, Willacy, Langer, & Velusamy 1998). The apparent structure may be due to chemical evolution. As a dense core collapses and the density increases, the photoionization and photodissociation processes become gradually less effective in the central region with highest density. The abundance of molecules sensitive to the photochemistry changes, and the CCS abundance decreases substantially (Suzuki et al. 1992). In addition, CCS depletes onto grains in a collapsing gas that increases the density (Bergin & Langer 1997), also explaining the lower abundance of CCS toward the center of L1544. These ideas of the chemical evolution are consistent with the result that L1544 is undergoing infall, as evidenced by kinematic tracers (see §4.2).

#### 4.2. Kinematical Structures of the CCS Condensation

As shown in §3, the kinematics of the CCS condensation are characterized by two major features: (1) blueshifted and redshifted components that coincide with each other along the line of sight, and (2) a velocity gradient along the major axis. Taking into account the flattened edge-on structure of the CCS condensation, the blueshifted and redshifted components may be explained by radial motion in the plane of the condensation, while the velocity gradient may represent

rotation of the condensation. One possible radial motion in the plane of the condensation is infall, which we favor over expansion, as discussed below. Here we consider the kinematics of the condensation using a simple model that consists of a spatially thin ring with both infall and rotation.

A simple model ring was obtained by modifying the model disk used in the study of the flattened envelope of L1527, which exhibits both infall and rotation (Ohashi et al. 1997). For L1544, we have modified the surface density distribution and velocity field in two ways: (1) The surface density is constant at  $R_{out} > R > R_{in}$ , and is null at  $R \leq R_{in}$ , where  $R_{out}$  and  $R_{in}$  are the outer and inner radii of the ring, respectively; (2) The infall velocity,  $V_{infall}$ , is constant throughout, while the rotation velocity,  $V_{rotation}$ , is proportional to the radius, i.e., rigid rotation such that  $V_{rotation} = V_{rotation}^0 (R/R_{out})$ , where  $V_{rotation}^0$  is the rotation velocity at  $R_{out}$ . The first modification makes the model have a ring structure. Under the assumption that the model ring has an edge-on configuration with respect to the observer, PV diagrams along the projected major axis of the model ring are calculated to compare with the observed PV diagram (Fig. 3a). For the model calculations,  $R_{out}$  was fixed at 15000 AU according to the CCS observations, while three parameters,  $R_{in}$ ,  $V_{infall}$ , and  $V_{rotation}^0$  remained adjustable.

As shown in Fig. 4a, when  $R_{in} = 7500$  AU,  $V_{infall} = 0.12$  km s<sup>-1</sup>, and  $V_{rotation}^0 = 0.09$  km s<sup>-1</sup>, the observed PV diagram (Fig. 3b) is well reproduced by the model: the calculated PV diagram shows a velocity structure, represented as a tilted ellipse, with a velocity difference at  $\Delta x = 0$  of 0.24 km s<sup>-1</sup> and a global velocity gradient of 0.09 km s<sup>-1</sup> per 15000 AU. Note that  $2V_{infall}$  corresponds to the velocity difference at  $\Delta x = 0$  in the calculated diagram, while  $V_{rotation}^0$  is equivalent to the velocity gradient per 15000 AU in the diagram. Hence, it is easily understood that much smaller or larger  $V_{infall}$  and/or  $V_{rotation}^0$  cannot reproduce the observed velocity structures. On the other hand, a ring structure with a larger  $R_{in}$  is essential for the model to reproduce the observed PV because when much smaller  $R_{in}$ , including the case of  $R_{in} = 0$  (equivalent to a model with a disk structure) is used, prominent peaks emerge close to  $\Delta x = 0$  in the calculated diagram (see Fig. 4b). This is because when  $R_{in}$  decreases, the total column density through the plane of the ring drastically increases close to  $\Delta x = 0$ .

One might argue that expansion instead of infall can explain the observed PV diagram. However, infall is more likely to explain the kinematics of the CCS condensation because the mass of L1544 derived from the virial theorem is comparable to or much smaller than that estimated from the 800  $\mu$ m dust emission: a virial mass is estimated to be  $\sim 1.7 M_{\odot}$  using the radius of the CCS condensation (15000 AU) and the mean line width of the CCS (0.4 km s<sup>-1</sup>), under the assumption of a spherical cloud with a constant density, while a mass of 2-6  $M_{\odot}$  was derived from 800  $\mu$ m dust emission<sup>3</sup> (T98). Inward motions in L1544 were also suggested from a spectroscopic method (T98, W99). Our result is remarkable as the observations resolve the velocity field and

---

<sup>3</sup>Note that the current CCS data is not adequate to derive a mass because CCS may be less abundant in the inner parts of L1544 (see §4.1).

show *direct* evidence for infall motions in the starless core L1544.

The kinematics of L1544 revealed by the CCS imaging show differences with the envelopes of YSOs. The estimated infall and rotation velocities are comparable to each other at a scale of 10000 AU, unlike YSOs where infall velocities are inferred to be 2 to 6 times larger than rotation velocities in the outer regions. In addition, the estimated infall velocity is much smaller in magnitude than those inferred around YSOs (e.g., Hayashi et al. 1993, Ohashi et al. 1997, Momose et al. 1998).

Although our model ring with a constant infall velocity and rigid rotation explain the kinematics of the CCS condensation very well, the current data do not place strong constraints on the radial dependences of the infall and rotation velocities because the CCS molecule traces only the outer part of the L1544 core. W99 have estimated infall and rotation velocities in the inner regions of L1544, where CCS emission is weak or absent, based on the self-absorption of  $\text{N}_2\text{H}^+$ . Their estimates of  $\sim 0.08 \text{ km s}^{-1}$  and  $\leq 0.14 \text{ km s}^{-1}$  for infall and rotation, respectively, suggests nearly constant infall and rotation throughout the L1544 core, from scales of 10000 to 1000 AU. The optical depth of the  $\text{N}_2\text{H}^+$  lines may yet mask the innermost regions of L1544, and direct measurements of the kinematics using an optically thin tracer may be valuable for revealing the radial dependences of the systematic motions in this starless core.

We are grateful to P. T. P. Ho, H. Masunaga, F. Nakamura, K. Saigo, S. Takano, and S. Yamamoto for fruitful discussions. We also thank H. Maezawa for his help during observations with the Nobeyama 45 m telescope.

## REFERENCES

- Beichman, C. A., Myers, P. C., Emerson, J. P., Harris, S., Mathieu, R., Benson, P. J., & Jennings, R. E. 1986, *ApJ*, 307, 337
- Benson, P. J., & Myers, P. C. 1989, *ApJS*, 71, 89
- Bergin E. A., & Langer, W. D. 1997, *ApJ*, 486, 316
- Carlstrom, J. E., Marshall, J., & Grego, L. 1996, *ApJ*, 456, L75
- Elias, J. H. 1978, *ApJ*, 224, 857
- Hayashi, M., Ohashi, N., & Miyama, S. M. 1993, *ApJ*, 418, L71
- Kuiper, T. B. H., Langer, W. D., & Velusamy, T. 1996, *ApJ*, 468, 761
- Langer, W. D., Velusamy, T., Kuiper, T. B., Levin, S., & Olsen, E. 1995, *ApJ*, 453, 293
- Matsumoto, T., Hanawa, T., & Nakamura, F. 1997, *ApJ*, 478, 569
- Momose, M., Ohashi, N., Kawabe, R., Nakano, T., & Hayashi, M. 1998, *ApJ*, 504, 314
- Myers, P. C., Fuller, G. A., Mathieu, R. D., Beichman, C. A., Benson, P. J., Schild, R. E., & Emerson, J. P. 1987, *ApJ*, 319, 340
- Nakamura, F., Hanawa, T., & Nakano, T. 1995, *ApJ*, 444, 770
- Ohashi, N. Hayashi, M., Ho, P. T. P., & Momose, M. 1997, *ApJ*, 475, 211
- Shu, F. H., Adams, F. C., & Lizano, S. 1987, *ARA&A*, 25, 23
- Suzuki, H., Yamamoto, S., Ohishi, M., Kaifu, N., Ishikawa, S., Hirahara, Y., & Takano, S. 1992, *ApJ*, 392, 551
- Tafalla, M., Mardones, D., Myers, P. C., Caselli, P., Bachiller, R., & Benson, P. J. 1998, *ApJ*, 504, 900 (T98)
- Ward-Thompson, D., Scott, P. F., Hills, R. E., and André, P. 1994, *MNRAS*, 268, 276
- Willacy, K, Langer, W. D., & Velusamy, T. 1998, *ApJ*, 507, L171
- Williams, J. P., Myers, P. C., Wilner, D. J., Di Francesco, J., 1999, *ApJ*, 513, L61 (W99)
- Wilner, D. J., & Welch, W. J. 1994, *ApJ*, 427, 898
- Wolkovitch, D., Langer, W. D., Goldsmith, P. F., & Heyer, M. 1997, *ApJ*, 477, 241
- Yamamoto, S., Saito, S., Kawaguchi, K., Chikada, Y., Suzuki, H., Kaifu, N., Ishikawa, S., & Ohishi, M. 1990, *ApJ*, 361, 318



Zhou, S., Evans, N. J., II, Kömpe, C., & Walmsley, C. M. 1993, ApJ, 404, 232

Fig. 1.— The CCS total intensity map observed with the BIMA array. The contour spacing is  $2\sigma$ , starting at  $\pm 2\sigma$  with  $1\sigma = 55 \text{ mJy beam}^{-1}$ . The cross indicates the peak position of the  $800 \mu\text{m}$  continuum emission (Ward-Thompson et al. 1994).

Fig. 2.— (*left panel*) Representative CCS channel maps. The contour spacing is  $2\sigma$ , starting at  $\pm 2\sigma$  with  $1\sigma = 165 \text{ mJy beam}^{-1}$ . (*right panel*) CCS line profiles of representative clumps (A and B) identified in the channel maps shown in the left panel. A double velocity component is obvious for each line profile. The arrows indicate the corresponding velocity component for each clump.

Fig. 3.— The observed PV diagrams. The contour spacing is  $2\sigma$ , starting at  $\pm 2\sigma$  with  $1\sigma = 165 \text{ mJy beam}^{-1}$ . The relative position ( $\Delta x$ ) was measured from [RA(2000)= $5^h 4^m 15^s 86$ , Dec(2000)= $25^\circ 10' 57''.6$ ]. The velocity is presented in the LSR frame, while the relative velocity ( $\Delta V$ ) measured from  $V_{LSR} = 7.24 \text{ km s}^{-1}$  is presented in the righthand axis for comparison with the model calculations. The two dashed lines indicate  $\Delta x = 0$  and  $\Delta V = 0$ . (*a*) The PV diagram along the projected minor axis (PA= $54^\circ$ ; line A-A' in Fig. 1). (*b*) The PV diagram along the projected major axis (PA= $144^\circ$ ; line B-B' in Fig. 1). The dashed curve shows a tilted ellipse, which represents the observed velocity structures.

Fig. 4.— The PV diagrams calculated two model rings. (*a*) The PV calculated with  $V_{infall} = 0.12 \text{ km s}^{-1}$ ,  $V_{rotation}^0 = 0.09 \text{ km s}^{-1}$ , and  $R_{in} = 7500 \text{ AU}$ . (*b*) The same as (*a*) but  $R_{in} = 2500 \text{ AU}$ .

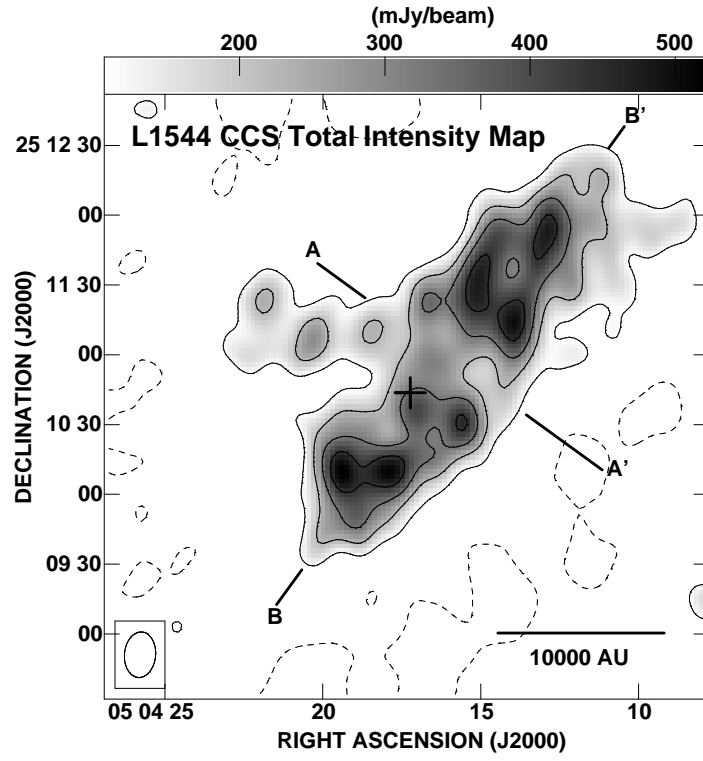
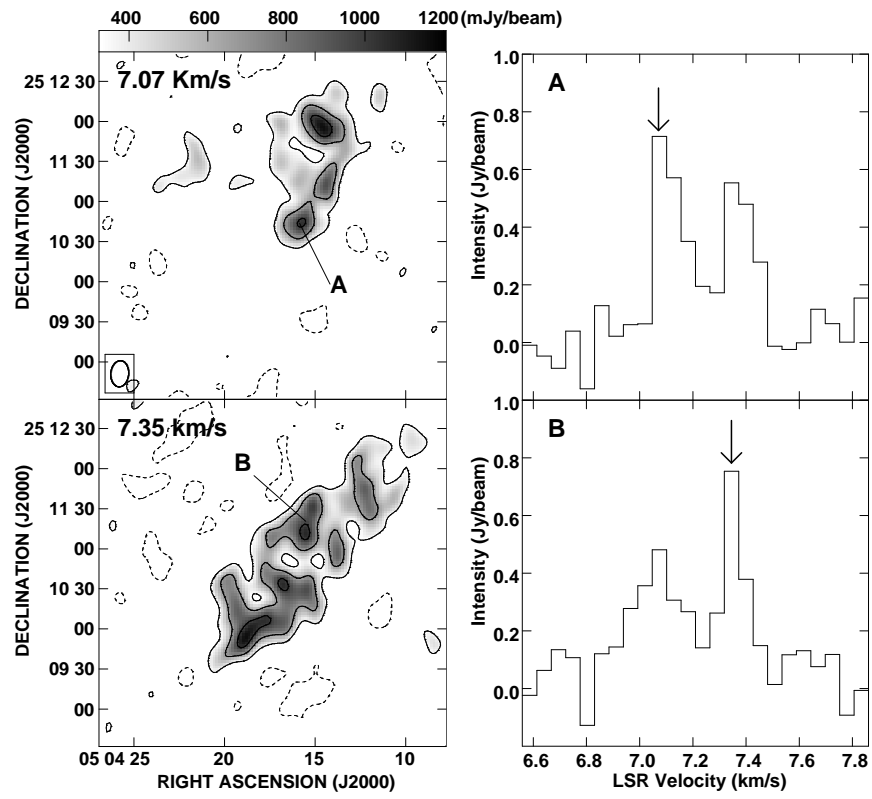


Fig. 1





**Fig. 2**

**Ohashi et al.**

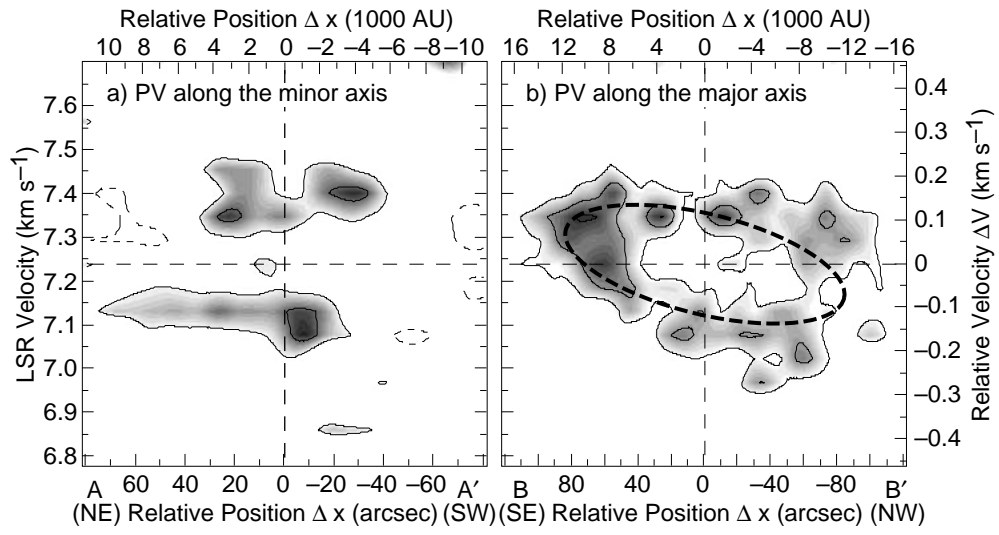


Fig. 3

Ohashi et al. (1999)

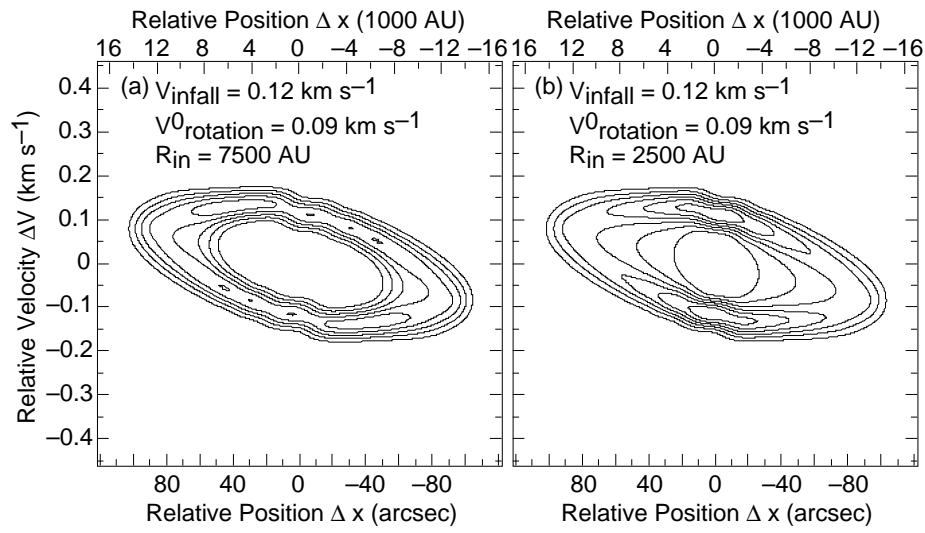


Fig. 4 Ohashi et al. (1999)